A Combined Model-Based and Data-Driven Multi-Fault Diagnosis Method for Series–Parallel Battery Packs

Tiantian Lin, Ziqiang Chen, *Senior Member, IEEE*, and Shiyao Zhou

***Abstract*—Multifault diagnosis is of great significance for the safe operation of lithium-ion battery (LIB) systems. A combined model-based and data-driven multifault diagnosis method based on an improved nonredundant cross-over voltage measurement topology is proposed for series–parallel connected LIB systems in this article. First, a reference module is selected and dual H-infinity filter is employed to estimate its state of charge (SOC). Rint model is adopted to evaluate the resistance inconsistency of modules. Second, Pearson correlation coefficients (PCCs) are calculated to detect faults considering inconsistencies in SOC and resistance between modules. The amplitude of auxiliary square wave is automatically determined based on the current variation. Standard deviation of voltage difference is employed to determine the threshold of PCCs. Finally, cell open-circuit (COC) faults, connection (CXN) faults, short-circuit (SC) faults and voltage sensor (VS) faults are comprehensively diagnosed. CXN faults and VS faults are identified according to the improved measurement topology and PCCs. Then, SC faults and COC faults are identified based on PCCs and fault modeling. The proposed method can also diagnose multiple faults that occur simultaneously or successively. The performance of the proposed diagnostic method is validated through experiments on a 2P-6S LIB pack.**

***Index Terms*—Correlation coefficients, dual H-infinity filter (DHIF), model-based, multifault diagnosis, series–parallel connected battery pack.**

I. Introduction

VEHICLE electrification has emerged as a critical driving force for the global green economy [1]. The lithium-ion battery (LIB) have been widely used in electric vehicles to their high power and energy density, long cycle life, and low self-discharge rate [2]. Fire and explosion accidents caused by battery system faults in electric vehicles are frequently reported. The safety issues of battery systems are receiving more and more attention. A reliable and efficient fault diagnosis method is essential for battery management system (BMS) to ensure the safe operation of LIB systems. A lot of efforts have been made to ensure the safety of LIB packs [3], [4]. Fault diagnosis methods mainly include two categories: model-based methods [5] and data-driven methods [6]. A comparison of the main methods currently used to diagnose faults in battery systems is given in Table I.

Observes and filters such as sliding mode observers [7], unscented Kalman filter (UKF) [8], extended Kalman filter (EKF) [9] and particle filter are usually used to estimate parameters and states in model-based diagnostic methods. Faults are detected by evaluating the residuals between model estimations and measured values. Luenberger observers and learning observers were constructed to diagnose and estimate the fault of increased internal resistance [10]. Sensor faults were diagnosed based on voltage residuals generated through an adaptive EKF [11]. Current sensor faults were diagnosed based on an improved equivalent circuit model with voltage as input and current as output using UKF [12]. Short-circuit (SC) faults were diagnosed based on the estimated charge-discharge capacity using EKF [13] and the SOC difference obtained using an H∞ nonlinear observer [14]. However, the computational burden of the model-based method is significant, which makes it difficult to apply onboard.

Data-driven methods mainly include machine learning based methods and signal processing based methods [15]. Recurrent neural network [16], convolutional neural network (CNN) [17] and support vector machine (SVM) [18] are the widely used machine learning algorithms. The long short-term memory neural network was used to estimate the surface temperature of the cell, and residuals were generated to detect thermal faults in [19]. False battery data were detected and classified based on CNN in [20]. Voltage fault was diagnosed based on discrete cosine filter and SVM, where the kernel function parameter and penalty factor were optimized using the grid search method [21]. However, some deep learning algorithms require massive amounts of historical data to train, resulting in high training costs. SVM works well with small samples, but performs poorly with large-scale training sets. Signal processing based methods, such as Shannon entropy [22], sample entropy [23] and Pearson correlation coefficient (PCC) [24], have low computational complexity and are easy to implement. Connection (CXN) faults were diagnosed based on entropy in [25]. Thermal abnormalities of LIB packs were detected and located based on spatiotemporal

Received 27 August 2024; revised 22 January 2025; accepted 25 February 2025. Date of publication 12 March 2025; date of current version 26 May 2025. Recommended for publication by Associate Editor D. Zhang. *(Corresponding author: Ziqiang Chen.)*

Tiantian Lin, Ziqiang Chen, and Shiyao Zhou are with the State Key Laboratory of Ocean Engineering, Shanghai Jiao Tong University, Shanghai 200240, China, and also with the Collaborative Innovation Center for Advanced Ship and Deep-Sea Exploration, Shanghai Jiao Tong University, Shanghai 200240, China (e-mail: ttlinet@sjtu.edu.cn; chenziqiang@sjtu.edu.cn; 569364453@sjtu.edu.cn).

Color versions of one or more figures in this article are available at https://doi.org/10.1109/TPEL.2025.3548643.

Digital Object Identifier 10.1109/TPEL.2025.3548643

TABLE I
COMPARISON OF FAULT DIAGNOSIS METHODS FOR BATTERY SYSTEMS

References	Methods	Fault types	Characteristics
[10]	Luenberger Observer	Increased internal resistance	Heavy computational burden
[11], [12]	Kalman filter	Sensor faults	Heavy computational burden
[13]	Kalman filter	SC faults	Heavy computational burden
[14]	H∞ nonlinear observer	SC faults	Heavy computational burden
[19]	Neural network	Thermal faults	High training costs, poor generalization ability
[21]	Support vector machine	Voltage fault	Performs poorly with large-scale training sets
[28]	Correlation coefficient	SC faults	Difficult to detect minor fault
[38], [39]	Correlation coefficient	COC faults	Difficult to detect minor fault
[25]	Entropy	CXN faults	Easily affected by noise
[26]	Entropy	Thermal abnormalities	Easily affected by noise
[27]	Entropy	SC faults	Easily affected by noise
[40]	Entropy	COC faults and SC faults	Easily affected by noise
[29], [30]	Model-based and data-driven fusion	Sensor faults and BIR faults	Heavy computational burden
[31], [34], [35]	Correlation coefficient	SC faults, VS faults and CXN faults	Increased hardware costs
[36]	Correlation coefficient	SC faults, thermal abuse faults, and CXN faults	Increased hardware costs
[37]	Correlation coefficient	VS faults and SC faults	Increased hardware costs

entropy in [26], where kernel density estimation was used to determine the threshold and entropy contribution function was designed to locate the abnormality. SC faults were diagnosed based on extremum sample entropy in [27] and PCCs in [28]. Signal processing based methods perform well in large battery systems, but it is difficult to detect small faults.

The aforementioned studies mainly focus on a certain type of fault and assume that other faults do not occur. However, there may be multiple faults in LIB packs that have similar effects on the behavior of LIBs but bring different levels of risk. It is necessary to distinguish between different types of faults.

There have been some studies focusing on multifault diagnosis of LIB packs. Sensor faults were estimated based on a model-based method with sliding mode observer, the battery internal resistance (BIR) fault were detected using a data-driven gap metric approach and isolated by combining the model-based and data-driven strategies [29]. The fault diagnosis scheme for parallel lithium-ion battery packs with main current sensor fault and BIR fault were presented in [30], where the fault-tolerant estimate for SOC were achieved. SC faults, voltage sensor (VS) faults and CXN faults were diagnosed based on PCCs, but the required voltage sensors were twice the number of cells in LIB packs [31]. Xia presented an improved interleaved voltage measurement topology where the total voltage of two adjacent cells were measured instead of the voltage of individual cells [32], [33]. The improved topology or its modified form, together with PCCs, has been widely used for multifault diagnosis. SC faults, VS faults and CXN faults were diagnosed in [34] and [35]. SC faults, thermal abuse faults and CXN faults were diagnosed in [36]. VS faults and SC faults were diagnosed in [37]. In these studies mentioned above, the multifault diagnosis was realized based on PCCs and the improved topology proposed by Xia et al. [32], [33] or its modified form. However, the voltages of individual cells were not measured in the improved topology or its modified form, creating an inconvenience for BMS management and increasing the safety risk. Cell open-circuit (COC) faults may also occur in series–parallel connected LIB packs. COC faults have a similar effect on the behavior of LIBs to SC faults, VS faults and CXN faults. Misdiagnosis can occur if COC faults are not taken into account. In addition, COC faults deteriorate inconsistencies in capacity and resistance between modules and limits the performance of LIB packs, which makes it necessary to diagnose COC faults. There is limited research related to COC faults. Zhou diagnosed COC faults based on PCCs [38], and compared the diagnostic performance of several different diagnostic methods for COC faults [39]. COC faults and SC faults were diagnosed based on modified sample entropy in [40]. Each increase in fault type increases the difficulty of fault diagnosis. Currently, a maximum of three fault types can be diagnosed. Almost all of them rely on special measurement topologies that increase the difficulty of BMS management. The limited types of faults diagnosed result in relatively low reliability of the diagnostic results. There are no studies that can comprehensively diagnose SC faults, VS faults, CXN faults, and COC faults.

This article presents a combined model-based and data-driven multifault diagnosis method for series–parallel connected LIB packs. To reduce the computational burden, a reference module is selected and dual H-infinity filter (DHIF) algorithm is employed to estimate the states of it, and the state of charge (SOC) of the other modules are derived according to the estimation results of the reference one. The main contributions of this article are summarized as follows.

1) The diagnostic speed and accuracy have been improved by improving the correlation-based method. First, model-based methods have been incorporated into correlation-based methods to evaluate and address inconsistencies between batteries. Second, a dynamic auxiliary waves have been introduced to replace the one with fixed amplitude. Finally, the PCC threshold has been dynamically adjusted based on inconsistencies.
2) An improved nonredundant cross-over voltage measurement topology that does not increase system or hardware complexity has been presented. This measurement topology is helpful for multifault diagnosis and does not increase the difficulty of BMS management.
3) Reliability of fault diagnosis results has been improved by comprehensively diagnosing SC faults, VS faults, CXN faults, and COC faults of series–parallel connected LIB packs. We have also considered situations where the faults of the same or different types occur simultaneously or sequentially. The size of faults has also been estimated

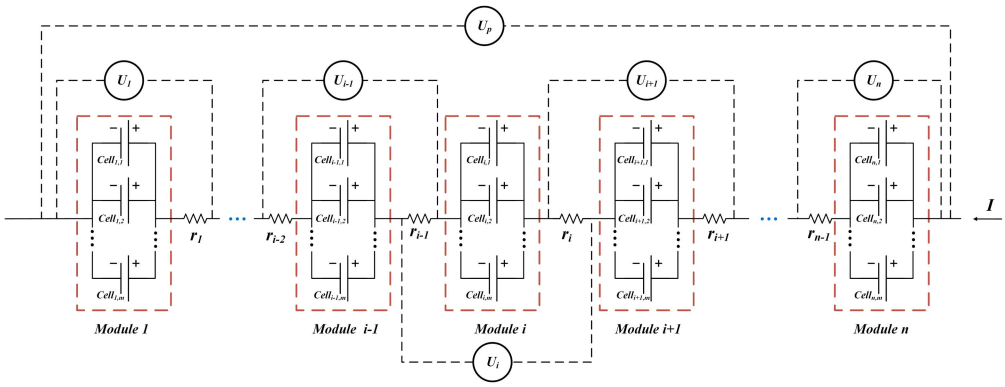

Fig. 1. Improved nonredundant cross-over voltage measurement topology.

with an estimation error of less than 10%. The performance of the proposed diagnostic method has been validated through experiments under the Federal urban driving schedule driving cycle (FUDS) on a 2P-6S LIB pack.

The remainder of this article is summarized as follows. The proposed multifault diagnosis method for series–parallel connected LIB packs is presented in Section II. The experimental setup and battery characteristic tests are introduced in Section III. The performance of the proposed diagnostic method is validated by experiments in Section IV. Finally, Section V concludes this article.

II. Diagnostic Method

A. Nonredundant Cross-Over Measurement Topology

A great number of cells are connected in series and/or parallel to meet power requirements in large-scale battery systems. Battery packs with mP-nS structure consist of n parallel modules connected in series and each parallel module consists of m cells connected in parallel. A parallel module consisting of several cells can be regarded as a large cell due to the same terminal voltage. A mP-nS battery pack can be regarded as a battery pack with n large cells connected in series. Modeling and state estimation are performed on large cells, namely parallel modules.

A variety of faults may occur in battery systems. Some faults have similar effects on the measured voltages, which may lead to misdiagnosis if there is no appropriate diagnostic method. A nonredundant cross-over measurement topology is proposed in this study to solve the multifault diagnostic problems, as shown in Fig. 1. One current sensor and $n + 1$ voltage sensors are needed to measure the current and voltages. The voltage sensor i ($i = 1, 2 \ \ldots \ n$) measures the total voltage of module i and its two adjacent wires. The voltage of the battery pack is also measured by the voltage sensor $n + 1$.

The relationship between voltage sensor readings and module voltages is shown in the following:

$$\begin{cases} U_i = V_i + I(r_{i-1} + r_i) + v_i \\ U_p = \sum_{i=1}^{n} V_i + \sum_{i=1}^{n-1} I r_i + v_p \end{cases} \tag{1}$$

where U_i ($i = 1,2,\ldots, n$) is the reading of voltage sensor i and V_i is the voltage of module i. U_p is measured voltage of the battery pack. r_i is resistance of the connection wire between module i and module $i + 1$. I is current of the battery pack which is positive when charging and v is the measurement noise.

As shown in (1), each connection resistance between two adjacent modules is associated with three voltage sensor readings, which makes it easy to distinguish CXN faults from other faults. If a CXN fault occurs, there are three measured voltages changing abnormally. A module voltage is associated with two voltage sensor readings. There are two measured voltages changing abnormally if an SC fault or a COC fault occurs. If a VS fault occurs, there is only one voltage sensor changing abnormally. For example, if a CXN fault occurs between module i and module $i + 1$, U_i, U_{i+1} and U_p show abnormal changes simultaneously. If an SC fault or a COC fault occurs on module i, both U_i and U_p show abnormal changes simultaneously. Only U_i shows abnormal changes if a VS fault occurs on the voltage sensor i.

B. Battery Modeling and State Estimation

It is impractical to perform accurate modeling and state estimation for each module considering the computational burden. A reference module is selected and the extensively used Thevenin model is utilized to describe its dynamics. The module with the lowest available capacity is selected as the reference one and is modeled as shown in Fig. 2(a), where U_{ocv} is the open-circuit voltage (OCV) and U_t is the terminal voltage. R_o, R_p, and C_p are the ohmic resistance, polarization resistance, and polarization capacitance, respectively. I is the current which is positive when charging. U_{ocv} is a function of SOC, as shown in (2), which can be acquired through OCV tests. SOC is the ratio of remaining capacity to maximum available capacity C_m, and can be calculated using (3), where the charging efficiency factor η is usually assumed to be a known constant [1]

$$U_{\text{ocv}} = h\,(\text{SOC}) \tag{2}$$

$$\text{SOC} = \text{SOC}_0 + \int_0^t \eta I\,(\tau)\,d\tau / C_m. \tag{3}$$

The discretized state space description is obtained as shown in (4), where state vector $x = [U_p, \text{SOC}]^{\text{T}}$, parameter vector

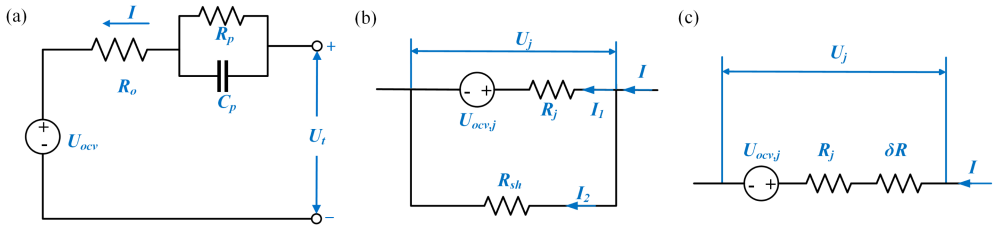

Fig. 2. Battery modeling. (a) Thevenin model. (b) Model of the parallel module with a short-circuit fault. (c) Model of the parallel module with a cell open-circuit fault.

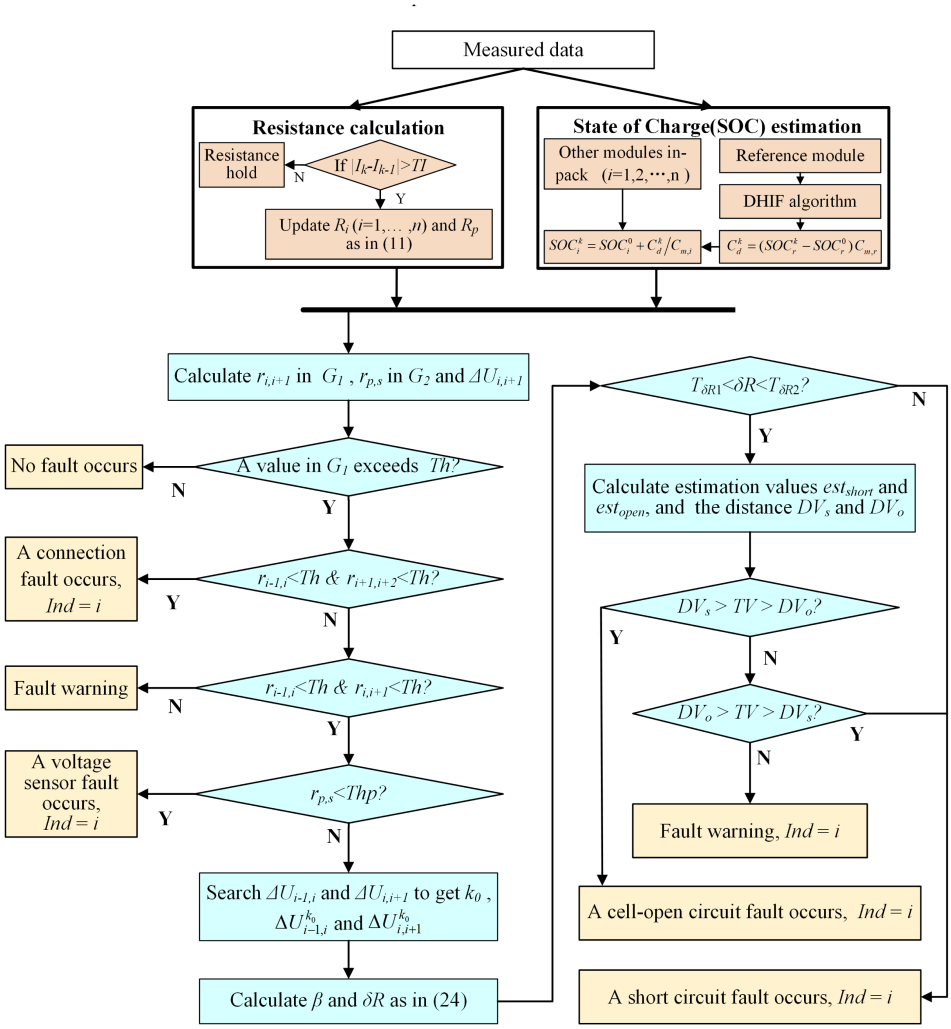

Fig. 3. Multifault diagnostic scheme.

$z = [R_o, R_p, C_p]^{\mathrm{T}}$, measurement vector $y = U_t$, matrix $A = \begin{bmatrix} e^{-\Delta t/\tau_p} & 0 \\ 0 & 1 \end{bmatrix}$, $B = \begin{bmatrix} (1 - e^{-\Delta t/\tau_p}) R_p \\ \eta \Delta t / C_m \end{bmatrix}$, $\tau_p = R_p C_p$, Δt is the sampling interval. $w_{x,k}$, $w_{z,k}$, and v_k are independent Gaussian noise vectors with covariance matrices Q_x, Q_z, and R, respectively.

The commonly used EKF algorithm requires that the probability density function of the noise is known and assumes that nature does not change the PDF of the noise, which is difficult to meet in practice, leading to a decrease in the robustness of the estimation and an increase in the maximum estimation error. Therefore, HIF, the robust version of EKF, is utilized. DHIF algorithm is adopted for parameter identification and state estimation to minimize the maximum estimation error. The calculation steps of DHIF algorithm are shown in Table II, where $P_{x,0}$, $Q_{x,k}$, $R_{x,k}$, $S_{x,k}$, $P_{z,0}$, $Q_{z,k}$, $R_{z,k}$, and $S_{z,k}$ are user-defined symmetric positive definite matrices, γ_x and γ_z are performance boundaries.

TABLE II
CALCULATION STEPS OF DHIF ALGORITHM

Step 1: Initialization:

For k=0, set the initial values: $\hat{x}_0 = E[x_0]$, $P_{x,0} = E[(x_0 - \hat{x}_0)(x_0 - \hat{x}_0)^T]$, $\hat{z}_0 = E[z_0]$, $P_{z,0} = E[(z_0 - \hat{z}_0)(z_0 - \hat{z}_0)^T]$, Q_x, Q_z, R_x, R_z, S_x, and S_z.

Step 2: Parameter estimation:

Prior estimation: $\hat{z}_k^- = \hat{z}_{k-1}$

Error covariance: $P_{z,k}^- = P_{z,k-1} + Q_z$

Error covariance update: $P_{z,k} = P_{z,k}^- \left(I - \gamma_z S_z P_{z,k}^- + C_{z,k}^T R_z^{-1} C_{z,k} P_{z,k}^-\right)^{-1}$

Gain matrix: $K_{z,k} = P_{z,k} C_{z,k}^T R_z^{-1}$

Estimation update: $e_{z,k} = y_k - \left[U_{ocv}(SO\hat{C}_{k-1}) + I_k \hat{R}_{o,k}^- + \hat{U}_{p,k-1}\right]$,

$\hat{z}_k = \hat{z}_k^- + K_{z,k} e_{z,k}$

Step 3: State estimation:

Prior estimation: $\hat{x}_k^- = A_k \hat{x}_{k-1} + B_k I_k$

Error covariance: $P_{x,k}^- = A_k P_{x,k-1} A_k^T + Q_x$

Error covariance update: $P_{x,k} = P_{x,k}^- \left(I - \gamma_x S_x P_{x,k}^- + C_{x,k}^T R_x^{-1} C_{x,k} P_{x,k}^-\right)^{-1}$

Gain matrix: $K_{x,k} = P_{x,k} C_{x,k}^T R_x^{-1}$

Estimation update: $e_{x,k} = y_k - \left[U_{ocv}(SO\hat{C}_k^-) + I_k \hat{R}_{o,k} + \hat{U}_{p,k}^-\right]$, $\hat{x}_k = \hat{x}_k^- + K_{x,k} e_{x,k}$

Step 4: Time update: k=k+1, return to step 2.

The matrices used are defined as follows:

$C_{x,k} = \left[1 \quad dU_{ocv}(SOC)/dSOC\big|_{x=\hat{x}^-}\right]$, $C_{z,k} = \left[I_k \quad D_k^R \quad D_k^C\right]$, $E_{RC} = e^{-\Delta t/\tau_p}\big|_{z=\hat{z}_k^-}$

$D_k^R = E_{RC}\Delta t\left(\hat{U}_{p,k-1}/R_p - I_k\right)/\tau_p\big|_{z=\hat{z}_k^-} + (1 - E_{RC}) I_k + E_{RC} D_{k-1}^R$,

$D_k^C = E_{RC}\Delta t\left(\hat{U}_{p,k-1}/R_p - I_k\right)/C_p^2\big|_{z=\hat{z}_k^-} + E_{RC} D_{k-1}^C$

The discharge capacity C_d can be calculated according to the estimated SOC of the reference module, as shown in (5). The SOCs of the remaining modules can be derived as shown in (6), where subscripts r and i refer to the reference module and module i, respectively. The superscript k refers to the kth sampling and 0 refers to the initial value. For example, $C_{m,i}$ refers to the maximum available capacity of module i

$$\begin{cases} x_k = A_{k-1} x_{k-1} + B_{k-1} I_k + w_{x,k} \\ z_k = z_{k-1} + w_{z,k} \\ y_k = U_{\text{ocv}}(\text{SOC}_k) + U_{p,k} + I_k R_{o,k} + v_k \end{cases} \tag{4}$$

$$C_d^k = (\text{SOC}_r^k - \text{SOC}_r^0) C_{m,r} \tag{5}$$

$$\text{SOC}_i^k = \text{SOC}_i^0 + C_d^k / C_{m,i}. \tag{6}$$

C. Fault Detection

Voltages show a linear correlation due to the same current input and similar battery characteristics. PCC which measures the linear relationship between two variables, is widely used for fault diagnosis of battery systems [41]. PCC is defined as follows:

$$r(X,Y) = \frac{\text{cov}(X,Y)}{\sigma_X \cdot \sigma_Y} = \frac{\sum_{i=1}^n (x_i - \bar{x})(y_i - \bar{y})}{\sqrt{\sum_{i=1}^n (x_i - \bar{x})^2} \sqrt{\sum_{i=1}^n (y_i - \bar{y})^2}} \tag{7}$$

where $r(X,Y)$ is PCC of variables X and Y, and cov(X,Y) is the covariance of the variables. σ_X and σ_Y denote the standard deviation of variables X and Y. $\bar{x}$ and $\bar{y}$ indicate the average of variables X and Y. The forgetting mechanism is adopted to avoid the effect of large amounts of historical data on PCC. The length of calculation window, denoted by w, is defined according to the measurement noise characteristics and the needs of fault diagnosis. Then, the recursive form of $r(X,Y)$ is obtained as shown in (8) and (9). Voltages fluctuate dramatically and the effect of measurement noise is negligible under dynamic conditions. When the current is zero, the measurement noise has a significant impact on PCC because voltages tend to stabilize and almost become horizontal lines.

When the current remains constant or changes little, the impact of measurement noise on PCC cannot be ignored either because the voltage fluctuation is small. A square wave with a fixed amplitude has been added to voltages to avoid an abnormal decrease in PCC caused by measurement noise [28], [34]. To ensure that PCC under noise-dominated conditions remains at the same level as that under dynamic conditions to avoid misdiagnosis, the amplitude of the square wave should be large enough. However, an increase in the amplitude weakens the dominance of voltage fluctuations on PCC under dynamic conditions, thereby reducing the sensitivity of detecting abnormal voltage drops. The square wave with variable amplitude was chosen considering the disadvantages of superimposing square waves with fixed amplitude. The wave amplitude W is determined based on current variation, as shown in (10). Where $a = 0.035$ and $b = 0.5$. The amplitude of the wave only needs to be calculated once according to (10) at each moment, regardless of the scale of battery packs. Therefore, the additional computational resources required are very small and do not affect real-time performance, even for large-scale battery packs.

The inconsistencies in resistance and SOC between modules are unavoidable and gradually increase. The impact of inconsistency makes the PCC slightly smaller than that when consistency is good. Rint model is adopted to evaluate the resistance inconsistency between modules. U_i can be modeled as $U_i = U_{\text{ocv},i} + IR_i$, where the subscript i denotes module i, R_i is the sum of the resistance of module i and its connection resistance at both ends. R_i can be calculated as shown in (11) and updated only when the current variation is large enough to reduce the effect of measurement noise on it. The PCC $r(U_i + W, U_j - I\Delta R_{i,j} + W)$ is calculated as the fault index instead of $r(U_i + W, U_j + W)$, so that the effect of resistance inconsistency is removed. Where $\Delta R_{i,j} = R_j - R_i$. When SOC-OCV curve is relatively flat, or when the slope is large but the curve is approximately straight, the effect of SOC inconsistency on PCC is small since PCC has the property $r(cX + d, Y) = r(X,Y)$, where c and d are constants. PCC will be reduced by SOC inconsistency when the SOC-OCV curve and its first-order derivatives change rapidly simultaneously. Different thresholds for PCC should be set based on SOC inconsistency to improve diagnostic speed and diagnostic accuracy.

The voltage difference $U_{i,j}$ is defined as (12), and it can be written as (13) according to Rint model. $U_{i,j}$ reflects the degree of OCV inconsistency between modules. The standard deviation of voltage difference, $SU_{i,j}$, is introduced to evaluate the OCV inconsistency between module i and module j within the calculation window, as in (14). The PCC threshold Th can

be decided according to $SU_{i,j}$. $U_{i,j}$ changes gradually because OCV changes gradually. Therefore, abrupt changes in $U_{i,j}$ are corrected when calculating $SU_{i,j}$ to avoid faults affecting the PCC threshold. The empirical equation between Th and $SU_{i,j}$ can be obtained through a large number of experiments, as shown in (15), where α_c is a constant

$$r(X,Y)_k = \frac{w\xi_{1,k} - \xi_{2,k}\xi_{3,k}}{\sqrt{w\xi_{4,k} - (\xi_{2,k})^2}\sqrt{w\xi_{5,k} - (\xi_{3,k})^2}} \tag{8}$$

$$\begin{cases} \xi_{1,k} = \xi_{1,k-1} + x_k y_k - x_{k-w} y_{k-w} \\ \xi_{2,k} = \xi_{2,k-1} + x_k - x_{k-w} \\ \xi_{3,k} = \xi_{3,k-1} + y_k - y_{k-w} \\ \xi_{4,k} = \xi_{4,k-1} + {x_k}^2 - {x_{k-w}}^2 \\ \xi_{5,k} = \xi_{5,k-1} + {y_k}^2 - {y_{k-w}}^2 \end{cases} \tag{9}$$

$$W_k = (-1)^k a\, e^{-b(I_k - I_{k-1})^2} \tag{10}$$

$$R_i^k = (U_i^k - U_i^{k-1})/(I_k - I_{k-1}) \tag{11}$$

$$U_{i,j} = U_j - I\Delta R_{i,j} - U_i \tag{12}$$

$$U_{i,j} = U_{\text{ocv},j} - U_{\text{ocv},i} \tag{13}$$

$$SU_{i,j}^k = \sqrt{\sum_{kt=k-w+1}^{k} \left(U_{i,j}^{kt} - \bar{U}_{i,j}\right)^2 \Big/ w} \tag{14}$$

$$\text{Th} = \sum_{c=0}^{3} \alpha_c (SU_{i,j})^c. \tag{15}$$

Fault detection can be achieved based on PCC. A fault is detected if two PCCs in G_1 exceed the corresponding threshold.

D. Fault Isolation

SC faults, COC faults, VS faults and CXN faults are comprehensively diagnosed based on PCCs and fault modeling. Two sets of PCCs should be calculated, as shown in (16). Where $r_{i,j} = r(U_i{+}W, U_j{-}I\Delta R_{ij}{+}W)$, $r_{p,s} = r(U_p{+}W, U_s{-}I\Delta R_{p,s}{+}W)$, and $U_s = \sum_{i=1}^{n} U_i$. G_1 and G_2 represent the set of PCCs between module voltages and the set of PCCs between total voltages, respectively. Since U_s contains double the connection resistance r_i, the resistance difference $\Delta R_{p,s}$ also needs to be subtracted when calculating $r_{p,s}$. The computation of $\Delta R_{p,s}$ is similar to that of ΔR_{ij}, and both are updated synchronously.

Both U_i and U_{i+1} contain the same fault information if a CXN fault occurs between module i and module $i+1$. As a result, $r_{i-1,i}$ and $r_{i+1,i+2}$ in G_1 will exceed the corresponding threshold, while $r_{i,i+1}$ remains within the threshold. If a fault other than a CXN fault occurs at location i, $r_{i-1,i}$ and $r_{i,i+1}$ in G_1 will exceed the corresponding threshold because neither U_{i-1} nor U_{i+1} contain fault information but U_i does. That makes it easy to distinguish CXN faults from the other types of faults. U_s contains fault information but U_p does not if a VS fault occurs at location i. Both U_s and U_p contain the same fault information if a COC or SC fault occurs at location i. Therefore, $r_{p,s}$ in G_2 is used to distinguish the VS fault from the other two types of faults. $r_{p,s}$ exceeds the corresponding threshold Thp when a VS fault occurs, but within the threshold Thp when the other two types of faults occur. Thus, the VS fault can be distinguished from the other two types of faults.

The voltage difference variation, $\Delta U_{i,j}$, is defined as (17), and it can be written as (18). $\Delta U_{i,j}$ is approximately equal to zero under normal conditions. There is an abrupt change in $\Delta U_{i,j}$ when a fault occurs. The scale of the fault can be evaluated according to $\Delta U_{i,j}$.

The module j can be modeled as shown in Fig. 2(b) after an SC fault occurs on module j. The electrical behavior can be expressed as (19), and U_j can be derived as (20), where β is the ratio of the equivalent SC resistance R_{sh} to R_j. Then, $\Delta U_{i,j}$ can be derived as (21), where k_0 refers to the moment when the fault occurs

$$\begin{cases} G_1 = \{r_{1,2}, r_{2,3}, \ldots, r_{n-1,n}, r_{n,1}\} \\ G_2 = \{r_{p,s}\} \end{cases} \tag{16}$$

$$\Delta U_{i,j}^k = U_{i,j}^k - U_{i,j}^{k-1} \tag{17}$$

$$\Delta U_{i,j}^k = (U_{\text{ocv},j}^k - U_{\text{ocv},i}^k) - (U_{\text{ocv},j}^{k-1} - U_{\text{ocv},i}^{k-1}) \tag{18}$$

$$\begin{cases} U_j = U_{\text{ocv},j} + I_1 R_j = I_2 R_{sh} \\ I = I_1 + I_2 \end{cases} \tag{19}$$

$$U_j = \beta(U_{\text{ocv},j} + IR_j)/(\beta + 1) \tag{20}$$

$$\Delta U_{i,j}^k = \begin{cases} -\left(I_k R_j + U_{\text{ocv},j}^k\right)/(\beta+1), & (k = k_0) \\ -(I_k - I_{k-1})\, R_j/(\beta+1), & (k > k_0) \end{cases} \tag{21}$$

$$U_j = U_{\text{ocv},j} + I\,(R_j + \delta R) \tag{22}$$

$$\Delta U_{i,j}^k = \begin{cases} I_k\, \delta R, & (k = k_0) \\ (I_k - I_{k-1})\, \delta R, & (k > k_0) \end{cases} \tag{23}$$

$$\begin{cases} \beta = -\left(I_k R_j + U_{\text{ocv},j}^{k_0}\right) \Big/ \Delta U_{i,j}^{k_0} - 1 \\ \delta R = \Delta U_{i,j}^{k_0} \Big/ I_{k_0} \end{cases} \tag{24}$$

$$\text{est}_{\text{short},k} = -(I_k - I_{k-1})\, R_j/(\beta+1) \quad k > k_0 \tag{25}$$

$$\text{est}_{\text{open},k} = (I_k - I_{k-1})\, \delta R \quad k > k_0 \tag{26}$$

$$\begin{cases} DV_{s,k} = \left|\text{est}_{\text{short},k} - \Delta U_{i,j}^k\right| \\ DV_{o,k} = \left|\text{est}_{\text{open},k} - \Delta U_{i,j}^k\right|. \end{cases} \tag{27}$$

The module capacity decreases and resistance increases after a COC fault occurs in module j. The value of resistance increase is defined as δR, and module j can be modeled as shown in Fig. 2(c). U_j and $\Delta U_{i,j}$ can be derived as (22) and (23), respectively, after a COC fault occurs in module j.

The moment when PCC first exceeds the threshold is noted as k_p. Searching for the first value of $\Delta U_{i,j}$ that exceeds the corresponding threshold TV near the k_p moment, and this value is $\Delta U_{i,j}^{k_0}$. β and δR can be calculated according to (24). The increase in resistance caused by the disconnection of any branch in the module is approximately equal to $mR/(m{-}1){-}R$, where R is the resistance of the parallel module with m cells connected in parallel. If δR is significantly less than $mR/(m{-}1){-}R$, the fault is diagnosed as an SC fault. Similarly, the fault is also diagnosed as an SC fault if δR significantly greater than $mR{-}R$. Otherwise, the values of $\Delta U_{i,j}$ under SC fault conditions and COC fault conditions when $k > k_0$ are estimated separately, and the estimated values are denoted as $\text{est}_{\text{short},k}$ and $\text{est}_{\text{open},k}$, respectively, as shown in (25) and (26). Calculating the distance

DV_s and DV_o between the estimated values and the actual value $\Delta U_{i,j}$, as shown in (27). A small DV_o indicates that the actual value $\Delta U_{i,j}$ is very close to the estimated value $\text{est}_{\text{open},k}$ for COC fault conditions. A small DV_s indicates that the actual value $\Delta U_{i,j}$ is very close to the estimated value $\text{est}_{\text{short},k}$ for SC fault conditions. It indicates that an SC fault has occurred if DV_s is small and DV_o is large, and vice versa, it indicates that a COC fault has occurred.

The proposed diagnostic scheme is shown in Fig. 3. Where *TI* is the threshold that determines whether to update the resistance R_i. $T_{\delta R1}$ and $T_{\delta R2}$ are the thresholds determined based on *mR*/(*m*–1)–*R* and *mR*–*R*, respectively. $n+1$ is replaced by 1 when it appears in subscripts. Ind refers to the location of the fault.

The voltage offset caused by the fault at location *i* is defined as δ_i. δ_i can be calculated as shown in (28), where $a_{i,k} = \Delta U^k_{i-1,i}$, $b_{i,k} = \Delta U^k_{i+1,i+2}$ if the fault at location *i* is a CXN fault, otherwise $b_{i,k} = \Delta U^k_{i,i+1}$. U_i, U_{i+1} and U_p all contain δ_i if a CXN fault occurs at location *i*. Both U_i and U_p contain δ_i if an SC fault or a COC occurs at location *i*. Only U_i contains δ_i if a VS fault occurs at location *i*. The PCC $r_{m,i}$ is defined as shown in (29). $r_{m,i}$ remains normal even if one of the following faults occurs: CXN fault, SC fault, COC fault, or VS fault (assuming only one fault occurs and Ind = *i*), because U_p and U_s-$I\Delta R_{p,s}$-δ_i contain the same fault information or neither contains fault information

$$\delta_{i,k} = \begin{cases} 0, & k < k_0 \\ \text{sign}\,(a_{i,k})\,(|a_{i,k}| + |b_{i,k}|)/2, & k = k_0 \\ \delta^l_{k-1} + \text{sign}\,(a_{i,k})\,(|a_{i,k}| + |b_{i,k}|)/2, & k > k_0 \end{cases} \tag{28}$$

$$r_{m,i} = r(U_p + W, U_s - I\Delta R_{p,s} - \delta_i + W). \tag{29}$$

The proposed method is also suitable for multiple faults that occur simultaneously or successively. Assuming two faults occur simultaneously, and the fault locations are *i* and *j*, respectively. The results are discussed in four cases.

Case 1: $r_{i-1,i}$, $r_{i+1,i+2}$, $r_{j-1,j}$ and $r_{j+1,j+2}$ are below the threshold Th. *Case 2:* $r_{i-1,i}$, $r_{i+1,i+2}$, $r_{j-1,j}$ and $r_{j,j+1}$ are below the threshold *Th*. *Case 3:* $r_{i-1,i}$, $r_{i,i+1}$, $r_{j-1,j}$ and $r_{j,j+1}$ are below the threshold Th, and $r_{p,s}$ remains normal. *Case 4*: $r_{i-1,i}$, $r_{i,i+1}$, $r_{j-1,j}$ and $r_{j,j+1}$ are below the threshold Th, and $r_{p,s}$ is below the threshold Th*p*.

In case 1, it can be concluded that the two faults are CXN faults.

In case 2, it can be concluded that the fault at location *i* is a CXN fault, and the fault at location *j* is not a CXN fault. Calculating $r_{m,i}$ as shown in (29). If $r_{m,i}$ is below the threshold Th*p*, it means that U_s-$I\Delta R_{p,s}$-δ_i contains the fault information δ_j while U_p does not, so it can be concluded that the fault at location *j* is a VS fault. Otherwise, the fault at location *j* is either an SC fault or a COC fault because both U_s-$I\Delta R_{p,s}$-δ_i and U_p contain the fault information δ_j, and then the fault type can be determined according to fault modeling.

In case 3, it can be concluded that the two faults are neither CXN faults nor VS faults. Then, fault modeling is performed to further determine the type of fault.

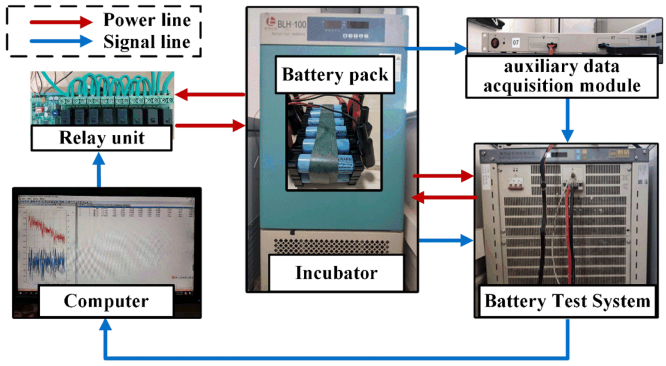

Fig. 4. Test bench for verification.

In case 4, it can be concluded that the two faults are not CXN faults and at least one of them is a VS fault. Therefore, at least one of $r_{m,l}$ ($l = i,j$) is below the threshold Th*p*. If both $r_{m,i}$ and $r_{m,j}$ are below the threshold Th*p*, the two faults are VS faults. If $r_{m,i}$ remains normal while $r_{m,j}$ is below the threshold Th*p*, the fault at location *i* is a VS fault and the fault at location *j* is an SC fault or a COC fault. Then the type of fault at location *j* is determined according to fault modeling. Conversely, the fault at location *j* is a VS fault and the type of fault at location *j* can be determined according to fault modeling.

If faults occur successively, the isolation principle is the same as above.

III. Experimental Design

A series of characteristic tests were conducted to obtain the necessary parameters of the module. A test bench was built up to validate the proposed method, as shown in Fig. 4. The battery test system acts as a charging and discharging device, and measures the voltage of pack and the current. Module voltages and the temperature were measured by the auxiliary data acquisition module. The measured data were sent to a computer. An incubator was employed to maintain the target temperature. The relay unit was used for circuit control. Twelve Li(NiCoAl)O_2/C 18 650 batteries with a nominal voltage of 3.7 V were connected in series and parallel to form a 2P-6S battery pack. The nominal capacity of cells is 3.2 Ah, and its operating voltage range is 2.75–4.2 V. The relay unit includes 8 relays, and is controlled by the computer. The measurement frequency was set to 1 Hz.

Capacity tests were carried out with a current of 0.5 C to obtain the maximum available capacity C_m. OCV tests were carried out with a current of 0.02 C to obtain the OCV–SOC curve. The results are shown in Fig. 5. The hybrid pulse power characterization test was also conducted to obtain characteristics of modules.

Extensive experiments were conducted on the 2P-6S battery pack to calibrate the thresholds mentioned above. The experiments were conducted under FUDS with a peak current of 2C. The length of the moving window was set to 80. Th*p*, $T_{\delta R1}$, $T_{\delta R2}$, and *TI* were set to 0.99998, 12 mΩ, 30 mΩ, and 10 A, respectively. Battery characteristics need to be taken into account when setting the thresholds. The PCC is extremely close to 1

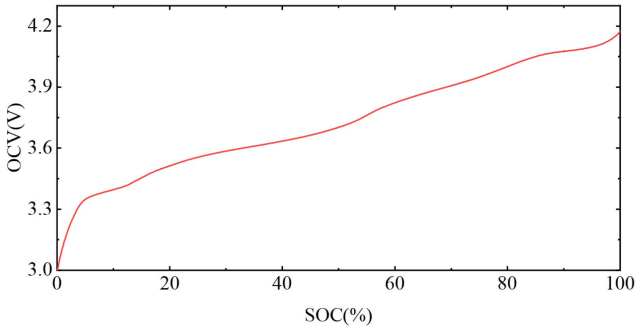

Fig. 5. OCV–SOC curve at 25 °C.

when modules are in good consistency. Th is set to 0.9999 if modules are in good consistency, that is $SOC_{i,j} \leq 1\%$, where $SOC_{i,j}$ is the SOC difference between module *i* and module *j*. If $SOC_{i,j} > 1\%$, Th is first set to 0.9999 and only updated according to (30) when PCC exceeds 0.9999, where $z = \min(SU_{i,j}, 1.82 \times 10^{-3})$. When SOC is less than 15%, OCV and resistance characteristics change greatly. SOC inconsistencies have a great impact on PCCs in this SOC intervals. The batteries are not fully activated when it starts working, and the characteristics are quite different if there is a SOC inconsistency. Therefore, special consideration is required for the first 330 s. Th is set to 0.99 if SOC $< 20\%$, to 0.995 for the first 330 seconds. *TV* is set to 50 mV if SOC $< 20\%$, to 15 mV for the first 330 s, to 4 mV if $SOC_{i,j} < 6\%$, otherwise *TV* is set to 5 mV.

In the fault diagnosis process, the SOC estimation results from the DHIF estimation are only used for interval division during fault diagnosis and the SOC estimation error is fully considered when setting the interval division related parameters to avoid the estimation error leading to misdiagnosis.

There may be a sudden offset at individual points due to problems of the acquisition equipment. When $\Delta U_{i,j}$ exceeds the threshold *TV* for the first time, the value of the previous moment is taken for the calculation to eliminate the influence of occasional offsets at individual points on the diagnosis and to avoid concealing the fault information

$$\mathrm{Th} = 9.89682z^3 - 499.506z^2 + 0.0500265z + 0.999967. \tag{30}$$

IV. Experimental Verification and Discussion

A. Fault Diagnosis of the Connection Fault

A CXN fault experiment was conducted at 20 °C. A resistor and a relay were connected in parallel, then were connected between module 3 and module 4. The relay switched from closed to open at 2000 s. A CXN fault occurred with a fault magnitude of 15.1 mΩ. The initial SOCs of modules were about 74%. The experimental results are shown in Fig. 6, where the PCCs are all obtained with superimposition of the square wave *W* shown in (10).

The maximum value of SOC residuals was 1.97%, and the minimum value of SOC during the experiment was above 20%. The values of $r_{2,3}$ and $r_{4,5}$ were 0.99395 and 0.99540 at 2001 s, as shown in Fig. 6(c). $r_{2,3}$ and $r_{4,5}$ simultaneously exceeded the corresponding threshold Th at 2001 s, while $r_{3,4}$ was 0.999998, higher than 0.99995. It means that a fault was detected and U_3 and U_4 contained exactly the same fault information, so the fault was a CXN fault. A fault was detected and identified as a CXN fault between module 3 and module 4 at 2001 s, and the fault diagnosis delay was 1 s. $\Delta U_{2,3}$ and $\Delta U_{4,5}$ exceeded the threshold *TV* for the first time at 2000 s, thus $k_0 = 2000$ s. The fault magnitude can be estimated according to $\Delta \bar{U}_{i,j}^{k_0}/I_{k_0}$, where $\Delta \bar{U}_{i,j}^{k_0}$ is the mean absolute value of $\Delta U_{2,3}^{k_0}$ and $\Delta U_{4,5}^{k_0}$. The estimation result was 13.9 mΩ, and the estimation error was 7.95%.

Thanks to the advantages of the proposed improved topology as shown in Fig. 1, CXN faults can be directly distinguished from the other types of faults based on whether the two abnormal PCCs in G_1 are adjacent. This isolation method is applicable not only to situations where the fault scale is constant, but also to situations where the fault scale varies randomly.

B. Fault Diagnosis of the Voltage Sensor Fault

A VS fault experiment was performed at 25 °C. The initial SOCs of six modules were 92.6%, 94.0%, 94.4%, 95.0%, 95.8% and 96.6%, respectively. A bias fault occurred on voltage sensor *6* at 3500 s, and the fault size was +6 mV.

The maximum value of SOC residuals was 2.70%, and the minimum value of SOC during the experiment was above 20%. Fig. 7(c) and (f) shows the calculated PCCs in group G_1. The PCC $r_{6,1}$ sometimes exceeded 0.9999 due to SOC inconsistency between module 1 and module 6. Th for it was updated according to (30) when $r_{6,1}$ exceeded 0.9999.

As shown in Fig. 7(f), The values of $r_{5,6}$ and $r_{6,1}$ were 0.99981 and 0.99978, and their thresholds were 0.9999 and 0.99980, respectively, at 3502 s. $r_{5,6}$ and $r_{6,1}$ simultaneously exceeded the corresponding threshold Th at 3502 s. A fault other than a CXN fault was detected at 3502 s and the fault location $Ind = 6$. $\Delta U_{5,6}$ and $\Delta U_{6,1}$ exceed the threshold *TV* for the first time at 3500 s, thus $k_0 = 3500$ s. The values of $r_{p,s}$ between 3500 and 3502 s were 0.999994, 0.999988, and 0.999985. Although the values were above the threshold Th*p*, there was a clear downward trend, so the fault was most likely to be a VS fault. $r_{p,s}$ continued to decrease and exceeded the threshold Th*p* at 3504 s. The fault was detected at 3502 s and identified as a VS fault at 3504 s. The fault diagnosis delay is 4 s. The absolute values of $\Delta U_{5,6}$ and $\Delta U_{6,1}$ at 3500 s were 5.76 and 6.03 mV, respectively. The estimated fault size was 5.895 mV, and the estimation error was 1.75%.

If two adjacent PCCs in G_1 show abnormalities, the possibility of CXN faults can first be ruled out as discussed above. If a COC or SC fault occurs, the changing trends of U_s and U_p are the same because they contain the same fault information. If a VS fault occurs, the changing trends of U_s and U_p are different because only U_s contains the fault information but U_p does not. Therefore, $r_{p,s}$ can be used to determine whether the fault is a VS fault. A VS fault is diagnosed if two adjacent PCCs in G_1 drop abnormally and at the same time $r_{p,s}$ drops abnormally. Once a VS fault has been diagnosed, the scale of the fault can be determined based on the corresponding $\Delta U_{i,j}^{k_0}$.

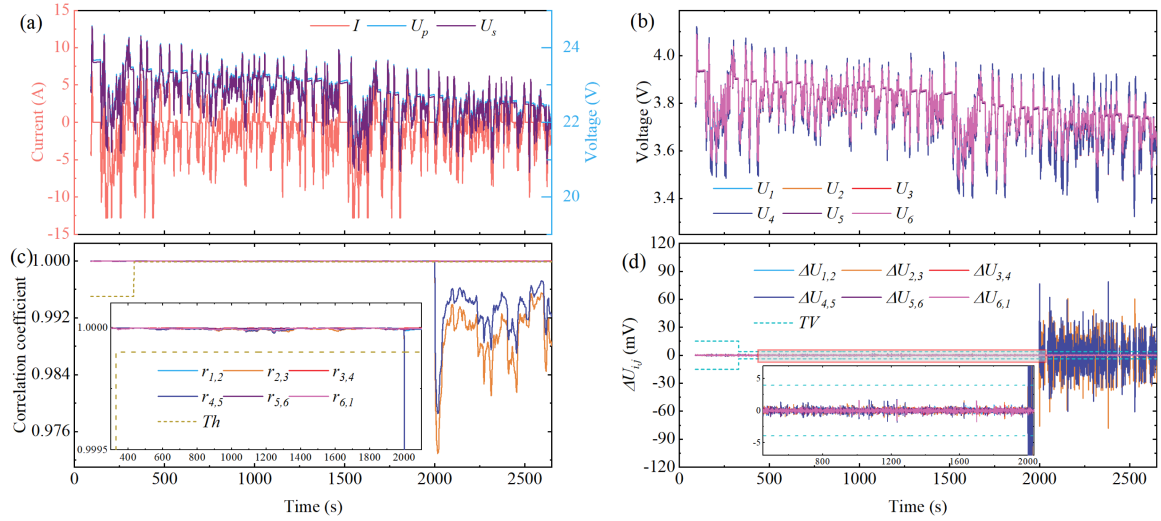

Fig. 6. Experimental results under connection fault conditions. (a) Currents and voltages of the battery pack. (b) Module voltages. (c) Correlation coefficients in group G_1. (d) Voltage difference variation, $\Delta U_{i,j}$, and the corresponding threshold TV.

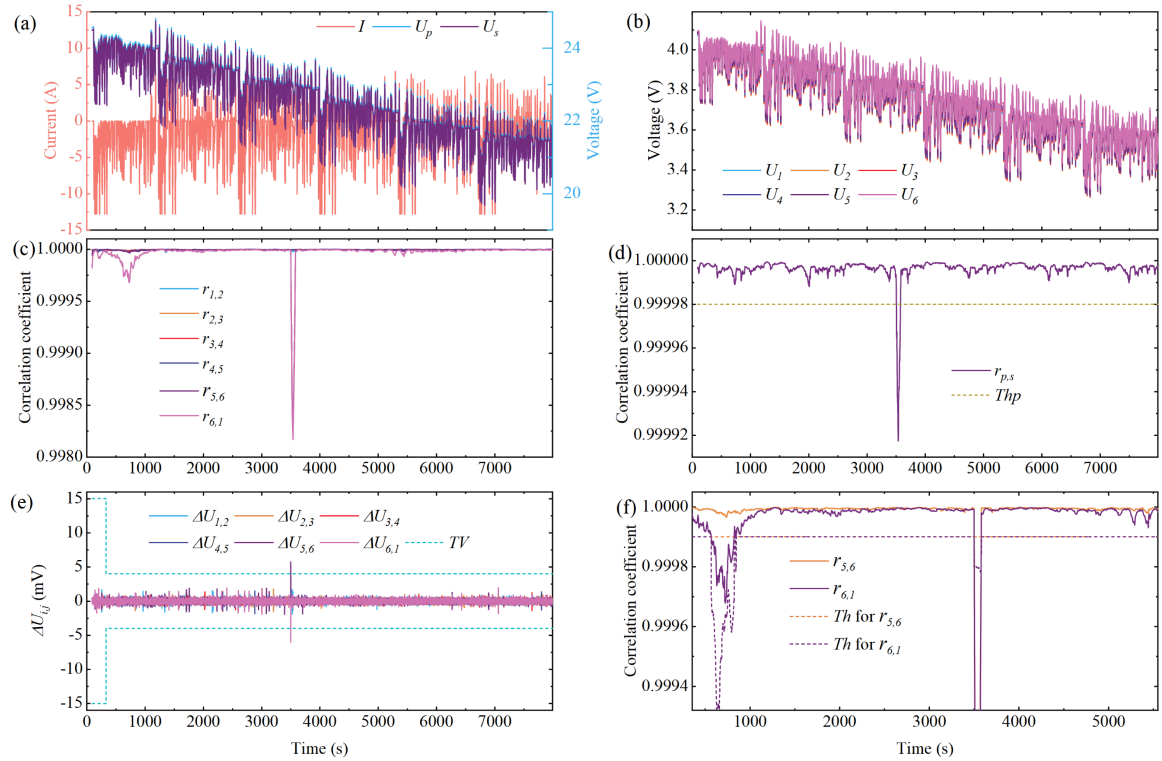

Fig. 7. Experimental results under voltage sensor fault conditions. (a) Currents and voltages of the battery pack. (b) Module voltages. (c) Correlation coefficients in group G_1. (d) Correlation coefficient in group G_2 and the corresponding thresholds. (e) Voltage difference variation, $\Delta U_{i,j}$, and the corresponding thresholds. (f) Correlation coefficients $r_{5,6}$ and $r_{6,1}$ and the corresponding thresholds.

C. Fault Diagnosis of the Module Short-Circuit Fault

An SC fault experiment was performed at 25 °C. A resistor of 9.1 Ω and a relay were connected in series, and they were connected in parallel with module 5 to perform SC fault experiments. The relay was closed at 1881 s, resulting in an SC fault on module 5. The relay was disconnected and the fault disappeared at 2115 s. The initial SOC of module 6 was approximately 94.4%, and SOCs of the other modules were approximately 96%. The experimental results are shown in Fig. 8.

The maximum value of SOC residuals was 2.30%, and the minimum value of SOC during the experiment was above 20%. As shown in Fig. 8(c) and (f), the PCC $r_{4,5}$ exceeded its threshold Th at 1882 s. The value of $r_{5,6}$ at 1882 s was 0.99986 which is lower than 0.9999, then the threshold for it was updated

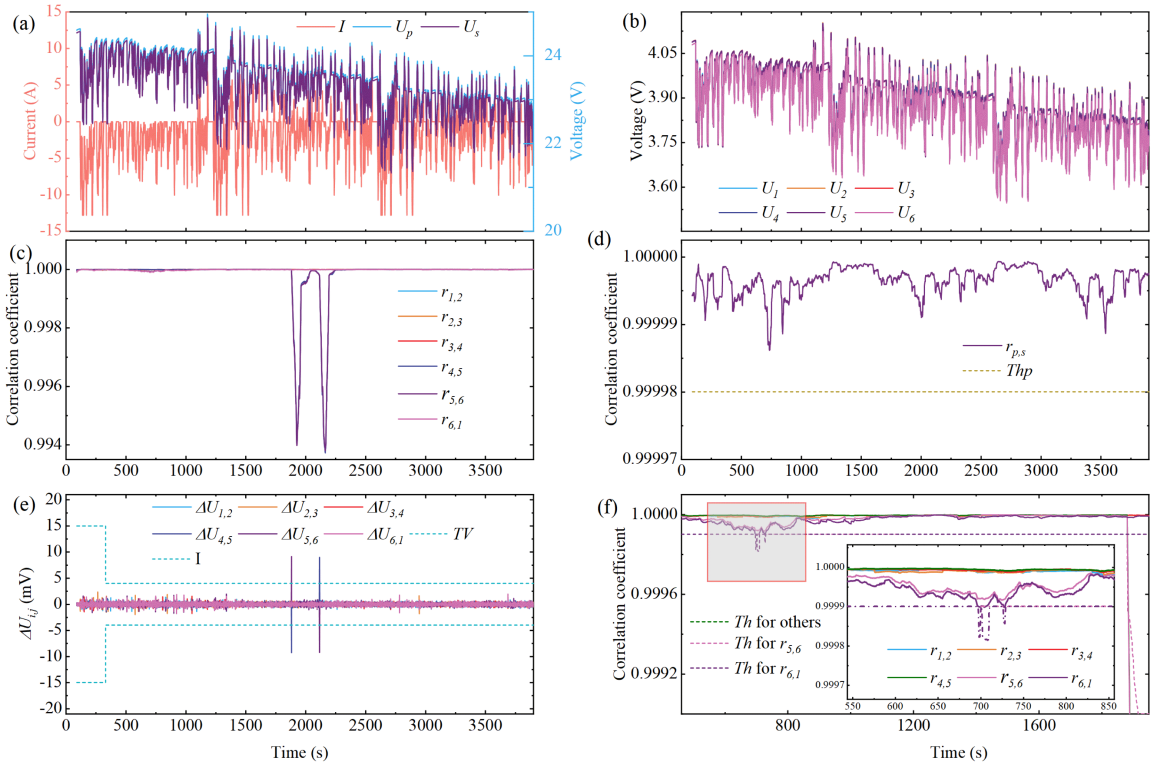

Fig. 8. Experimental results under module short-circuit fault conditions. (a) Currents and voltages of the battery pack. (b) Module voltages. (c) Correlation coefficients in group G_1. (d) Correlation coefficient in group G_2. (e) Voltage difference variation, $\Delta U_{i,j}$, and the corresponding thresholds. (f) Correlation coefficients in group G_1 and the corresponding thresholds.

TABLE III
ESTIMATION RESULTS UNDER A SHORT-CIRCUIT FAULT CONDITION

k (s)	$\Delta\bar{U}_{i,j}$ (mV)	$\text{est}_{\text{short}}$ (mV)	est_{open} (mV)	DV_s (mV)	DV_o (mV)
1882	0.350	0	0	0.350	0.350
1883	0.184	0.0840	33.5	0.100	33.3
1884	0.264	0.0564	22.5	0.208	22.2
1885	0.0870	0.0552	22.0	0.0318	21.9

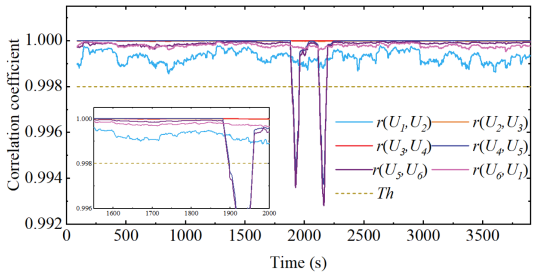

Fig. 9 Calculation results of regular correlation coefficients.

according to (30) and the result was 0.99951. A fault warning was given because only $r_{4,5}$ exceeded the corresponding threshold at 1882 s. The PCC $r_{5,6}$ exceeded its threshold Th at 1885 s. Therefore a fault other than a CXN fault was detected at 1885 s and Ind = 5. $\Delta U_{4,5}$ and $\Delta U_{5,6}$ exceeded the threshold TV for the first time at 1881 s, indicating that $k_0 = 1881$ s. The values of $r_{p,s}$ between 1881 s and 1885 s were all around 0.999997, which were above the threshold Thp and did not show a decreasing trend. Thus the fault was not a VS fault. According to (24), β and δR were calculated to be 430.5 and 20.64 mΩ respectively. The estimated values $\text{est}_{\text{short},k}$ and $\text{est}_{\text{open},k}$, and the estimated distance $DV_{s,k}$ and $DV_{o,k}$ were calculated according to (25)–(27) where $k > k_0$. The estimation results are listed in Table III. Where $\Delta\bar{U}_{i,j}$ is the mean absolute value of $\Delta U_{4,5}$ and $\Delta U_{5,6}$. An SC fault is confirmed since $DV_o > TV > DV_s$. The fault was warned at 1882 s and diagnosed as an SC fault at 1885 s. The fault diagnosis delay is 4 s. $\beta \cdot R_{\text{Ind}}^{k_0}$ is the estimated equivalent SC resistance, and the estimation value is 9.608 Ω. The estimation error is 5.58%.

The existing correlation-based method ignores the impact of inconsistency [34], [35]. The PCCs without considering inconsistencies for the SC fault experiment are shown in Fig. 9. When the fault does not occur, the minimum value of the regular PCCs is 0.998546, while the minimum value of the modified PCCs with inconsistency processing is 0.999895. It can be seen that the inconsistencies between batteries affect the calculation results of the PCCs. The threshold for regular PCCs is set to 0.998. The PCCs $r(U_4,U_5)$ and $r(U_5,U_6)$ exceed the threshold at 1898 and 1896 s, respectively, and the fault detection delay is 17 s. The fault detection delay in this paper is 4 s. The fault detection speed is significantly improved. It is difficult for regular PCCs to exceed the threshold if the fault scale is smaller, resulting

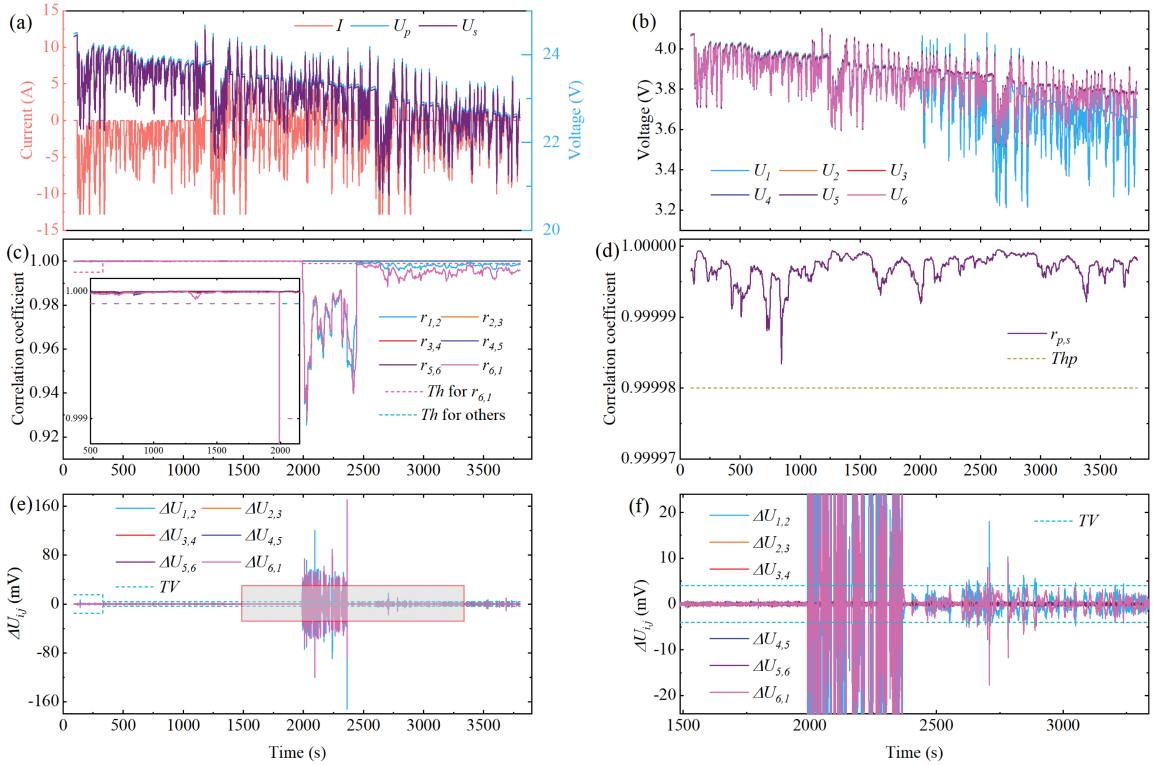

Fig. 10. Experimental results under cell open-circuit fault conditions. (a) Currents and voltages of the battery pack. (b) Module voltages. (c) Correlation coefficients in group G_1. (d) Correlation coefficient in group G_2. (e) Voltage difference variation, $\Delta U_{i,j}$, and the corresponding thresholds. (f) Local magnification of $\Delta U_{i,j}$, and the corresponding thresholds.

in lower diagnostic accuracy. It is worth noting that the regular PCCs under the fault-free conditions may also be lower than 0.998 when the inconsistencies between batteries are more severe, resulting in misdiagnosis.

D. Fault Diagnosis of the Cell Open-Circuit Fault

A COC fault experiment was performed at 25 °C. A relay was connected in module 1 in the COC fault experiment. The initial SOCs of modules were about 92%, with a maximum SOC difference of 1.62%. The relay was disconnected at 1991 s, and a COC fault occurred in module 1. The experimental results are shown in Fig. 10.

The maximum value of SOC residuals was 2.64%, and the minimum value of SOC during the experiment was above 20%. As shown in Fig. 10(c), the PCCs $r_{1,2}$ and $r_{6,1}$ simultaneously exceeded the corresponding thresholds Th at 1992 s. Therefore, a fault other than a CXN fault was detected at 1992 s and Ind = 1. $\Delta U_{1,2}$ and $\Delta U_{6,1}$ exceeded the threshold *TV* for the first time at 1991 s, thus $k_0 = 1991$ s. This may be an SC fault or COC fault as there is no significant downward trend in $r_{p,s}$ and $r_{p,s} >$ Th*p*, as shown in Fig. 10(d). According to (24), β and δR were calculated to be 108.2 and 20.67 mΩ respectively. The estimated values $\text{est}_{\text{short},k}$ and $est_{\text{open},k}$, and the estimated distance $DV_{s,k}$ and $DV_{o,k}$ were calculated according to (25)–(27) where $k > k_0$. The estimation results are listed in Table IV. Where $\Delta\bar{U}_{i,j}$ is the mean absolute value of $\Delta U_{1,2}$ and $\Delta U_{6,1}$. When $k =$ 1992 s, the values of $\text{est}_{\text{short},k}$ and $\text{est}_{\text{open},k}$ were close to each other and both were below the threshold *TV* since the current was almost the same as that at the previous moment, and it was difficult to determine whether the fault was an SC fault or a COC fault. A COC fault was confirmed since $DV_s > TV > DV_o$ when $k = 1993$ s. A fault other than a CXN fault and a VS fault was detected and the fault location was identified at 1992 s, and it was identified as a COC fault at 1993 s. The fault diagnosis delay is 2 s.

TABLE IV
ESTIMATION RESULTS UNDER A CELL OPEN-CIRCUIT FAULT CONDITION

k (s)	$\Delta\bar{U}_{i,j}$ (mV)	$\text{est}_{\text{short}}$ (mV)	est_{open} (mV)	DV_s (mV)	DV_o (mV)
1992	2.02	0.00350	0.385	2.02	1.64
1993	6.00	0.0520	5.64	5.95	0.360
1994	43.1	0.409	44.3	42.7	1.20

The resistance R_i was updated at 2364 s, therefore the fluctuations in $\Delta U_{1,2}$ and $\Delta U_{6,1}$ decrease immediately after 2364 s, but they still frequently exceed the threshold *TV* due to the significant inconsistencies between module 1 and the other modules. The values of $r_{1,2}$ and $r_{6,1}$ after 2443 s are closer to 1 compared to before.

E. Fault Diagnosis of the Multiple Fault

The multifault experiment was performed at 20 °C, and the initial SOCs of six modules were approximately 84%. An SC fault occurred on module 5 at 4479 s and the SC resistance was 6.1 Ω. A COC fault occurred in module 1 at 5376 s.

TABLE V
ESTIMATION RESULTS OF THE MULTIFAULT EXPERIMENT

k (s)	$\Delta\bar{U}_{i,j}$ (mV)	$\text{est}_{\text{short}}$ (mV)	est_{open} (mV)	DV_s (mV)	DV_o (mV)
4480	0.497	0.346	76.8	0.151	76.3
4481	0.374	0.036	8.00	0.338	7.62
4482	0.205	0.093	20.6	0.112	20.4

TABLE VI
ESTIMATION RESULTS OF THE MULTIFAULT EXPERIMENT—PART 2

k (s)	$\Delta\bar{U}_{i,j}$ (mV)	$\text{est}_{\text{short}}$ (mV)	est_{open} (mV)	DV_s (mV)	DV_o (mV)
5377	33.9	0.079	33.9	33.8	0.0254
5378	0.800	0.000	0.000	0.800	0.800
5379	1.10	0.000	0.000	1.10	1.10

The maximum value of SOC residuals was 2.36%, and the minimum value of SOC during the experiment was above 20%. The values of $r_{4,5}$ and $r_{5,6}$ were 0.999871 and 0.999866, respectively, at 4480 s, and both were below the corresponding thresholds *Th*. Therefore, a fault other than a CXN fault was detected at 4480 s and Ind = 5. $\Delta U_{4,5}$ and $\Delta U_{5,6}$ exceeded the threshold *TV* for the first time at 4479 s, indicating that k_0 = 4479 s. The values of $r_{p,s}$ between 4479 s and 4480 s were all around 0.999999, which were above the threshold Th*p* and did not show a decreasing trend. Therefore, the fault was not a VS fault, but an SC fault or a COC fault. According to (24), β and δR were calculated to be 270.1 and 18.42 mΩ, respectively. The estimated values $\text{est}_{\text{short},k}$ and $\text{est}_{\text{open},k}$, and the estimated distance $DV_{s,k}$ and $DV_{o,k}$ were calculated according to (25)–(27) where $k > k_0$. The estimation results are listed in Table V. Where $\Delta\bar{U}_{i,j}$ is the mean absolute value of $\Delta U_{4,5}$ and $\Delta U_{5,6}$. An SC fault was confirmed since $DV_o > TV > DV_s$ when $k = 4480$ s. The SC fault was diagnosed at 4480 s and the fault diagnosis delay was 1 s. $\beta \cdot R_{Ind}^{k_0}$ is the estimated equivalent SC resistance, and the estimation value is 6.084 Ω. The estimation error is 0.26%.

The values of $r_{1,2}$ and $r_{6,1}$ were 0.998867 and 0.998857, respectively, at 5377 s, and both were below the corresponding thresholds Th. Therefore, a fault other than a CXN fault was detected at 5377 s and Ind = 1. $\Delta U_{1,2}$ and $\Delta U_{6,1}$ exceeded the threshold *TV* for the first time at 5376 s, indicating that k_0 = 5376 s. The values of $r_{p,s}$ between 5376 s and 5377 s were all around 0.999996, which were above the threshold Th*p* and did not show a decreasing trend. Therefore, the fault was not a VS fault, but an SC fault or a COC fault. According to (24), β and δR were calculated to be 407.5 and 21.69 mΩ respectively. The estimated values $\text{est}_{\text{short},k}$ and $\text{est}_{\text{open},k}$, and the estimated distance $DV_{s,k}$ and $DV_{o,k}$ were calculated according to (25)–(27) where $k > k_0$. The estimation results are listed in Table VI. Where $\Delta\bar{U}_{i,j}$ is the mean absolute value of $\Delta U_{1,2}$ and $\Delta U_{6,1}$. A COC fault was confirmed since $DV_s > TV > DV_o$ when $k = 5377$ s. The COC fault was diagnosed at 5377 s and the fault diagnosis delay was 1 s.

The SC fault occurred on module 5 was diagnosed accurately at 4480 s, and the COC fault occurred in module 1 was diagnosed accurately at 5377 s. The fault diagnosis delays were both 1 s.

Thanks to the advantages of the proposed improved topology as shown in Fig. 1, it can be first determined if it is a CXN fault based on the location of the abnormal PCCs in G_1. It can be determined if it is a VS fault according to $r_{p,s}$ after the possibility of CXN faults has been ruled out. SC faults and COC faults can be distinguished based on fault modeling after the possibility of CXN and VS faults have been ruled out. The fault experiments have demonstrated the reliability of the multifault diagnosis method for CXN faults, VS faults, SC faults and COC faults. The results of a large number of fault experiments demonstrate that faults with a scale larger than 5 mV can be diagnosed quickly and accurately, and the diagnostic delay is generally a few seconds. The diagnostic delay of the regular PCC-based method is usually tens of seconds or even longer, and there are cases of missed diagnosis and misdiagnosis.

The proposed diagnosis method performs well in terms of computational cost, diagnostic accuracy and speed, making it suitable for online applications. Zhou's [39] comparative study has shown that the regular PCC-based method outperforms the model-based method in terms of diagnostic accuracy and response. The diagnostic accuracy and response of the proposed method is better than that of the regular PCC-based method, which has been proven by experiments in this article. The computational cost of the proposed method is much lower compared to model-based methods. For an *m*P-*n*S LIB pack, DHIF algorithm only needs to be executed once and $n + 1$ PCCs should be calculated. A simulation dataset of a 2P-96S LIB pack was used for offline calculation, with each of the 96 module voltages containing 10 000 data points. MATLAB was utilized to carry out the calculation and the CPU used was Intel(R) Core(TM) i5-8400. The calculation was repeated three times and the average calculation time was 1.417 s, of which DHIF algorithm took 0.434 s and the rest took 0.983 s. The computational cost of PCCs is much lower compared to DHIF algorithm. DHIF algorithm needs to be executed 96 times for model-based methods, and the total computational cost is much higher compared to the proposed method.

V. CONCLUSION

This article proposed a combined model-based and data-driven multifault diagnosis method for series–parallel connected LIB packs. The main contribution of this work is that SC faults, VS faults, CXN faults and COC faults of series–parallel connected LIB packs are comprehensively diagnosed based on the proposed improved nonredundant cross-over voltage measurement topology. The proposed diagnosis method performs well in terms of computational cost, diagnostic accuracy and speed. The proposed measurement topology does not increase system or hardware complexity. The amplitude of auxiliary wave is automatically determined based on the current variation, inconsistencies in SOC and resistance were considered, and standard deviation of voltage difference was employed to calculate the thresholds for PCCs in order to improve diagnostic accuracy and speed. VS faults and CXN faults were distinguished according to PCCs and the proposed measurement topology. Then, SC faults and COC faults were distinguished according to PCCs and fault

modeling. The size of faults was estimated and the maximum estimate error was less than 10%. The proposed method can also diagnose multiple faults that occur simultaneously or successively. This article mainly focused on the abrupt faults. The proposed method works well for the diagnosis of abrupt faults, but there is room for improvement in the diagnosis of gradual faults. In the future, we will put more effort into the diagnosis of gradual faults.

REFERENCES

[1] D. Zhang, J. Jiang, and W. Zhang, "Load prediction and distributed optimal control of on-board battery systems for dual-source trolleybuses," *IEEE Trans. Transp. Electrific.*, vol. 3, no. 1, pp. 284–296, Mar. 2017.

[2] L. Lu, X. Han, J. Li, J. Hua, and M. Ouyang, "A review on the key issues for lithium-ion battery management in electric vehicles," *J. Power Sources*, vol. 226, pp. 272–288, 2013, doi: 10.1016/j.jpowsour.2012.10.060.

[3] F. Peng, S. Jiang, Y. Zhao, and L. Ren, "Soft short-circuit fault diagnosis for vehicular battery packs with interpretable full-dimensional statistical analytics," *IEEE Trans. Power Electron.*, vol. 39, no. 9, pp. 11650–11664, Sep. 2024.

[4] G. Li, B. Li, S. Wang, P. Chen, C. Li, and B. Liu, "A fast model-free method for identifying internal short circuit resistance in Lithium-ion battery," *IEEE Trans. Power Electron.*, vol. 40, no. 3, pp. 4557–4568, Mar. 2025.

[5] M. Schmid, E. Gebauer, C. Hanzl, and C. Endisch, "Active model-based fault diagnosis in reconfigurable battery systems," *IEEE Trans. Power Electron.*, vol. 36, no. 3, pp. 2584–2597, Mar. 2021, doi: 10.1109/tpel.2020.3012964.

[6] Y. Zhao, P. Liu, Z. Wang, L. Zhang, and J. Hong, "Fault and defect diagnosis of battery for electric vehicles based on big data analysis methods," *Appl. Energy*, vol. 207, pp. 354–362, 2017, doi: 10.1016/j.apenergy.2017.05.139.

[7] S. Dey, S. Mohon, P. Pisu, and B. Ayalew, "Sensor fault detection, isolation, and estimation in Lithium-Ion batteries," *IEEE Trans. Control Syst. Technol.*, vol. 24, no. 6, pp. 2141–2149, Nov. 2016, doi: 10.1109/tcst.2016.2538200.

[8] M. Partovibakhsh and L. Guangjun, "An adaptive unscented kalman filtering approach for online estimation of model parameters and State-of-charge of Lithium-Ion batteries for autonomous mobile robots," *IEEE Trans. Control Syst. Technol.*, vol. 23, no. 1, pp. 357–363, Jan. 2015, doi: 10.1109/tcst.2014.2317781.

[9] G. L. Plett, "Extended Kalman filtering for battery management systems of LiPB-based HEV battery packs," *J. Power Sources*, vol. 134, no. 2, pp. 262–276, 2004, doi: 10.1016/j.jpowsour.2004.02.032.

[10] W. Chen, W.-T. Chen, M. Saif, M.-F. Li, and H. Wu, "Simultaneous fault isolation and estimation of lithium-ion batteries via synthesized design of luenberger and learning observers," *IEEE Trans. Control Syst. Technol.*, vol. 22, no. 1, pp. 290–298, Jan. 2014, doi: 10.1109/tcst.2013.2239296.

[11] Z. Liu and H. He, "Sensor fault detection and isolation for a lithium-ion battery pack in electric vehicles using adaptive extended Kalman filter," *Appl. Energy*, vol. 185, pp. 2033–2044, 2017, doi: 10.1016/j.apenergy.2015.10.168.

[12] Q. Yu, L. Dai, R. Xiong, Z. Chen, X. Zhang, and W. Shen, "Current sensor fault diagnosis method based on an improved equivalent circuit battery model," *Appl. Energy*, vol. 310, 2022, Art. no. 118588, doi: 10.1016/j.apenergy.2022.118588.

[13] Y. Zheng, A. Shen, X. Han, and M. Ouyang, "Quantitative short circuit identification for single Lithium-Ion cell applications based on charge and discharge capacity estimation," *J. Power Sources*, vol. 517, 2022, Art. no. 230716, doi: 10.1016/j.jpowsour.2021.230716.

[14] Y. Xu, X. Ge, W. Shen, and R. Yang, "A soft short-circuit diagnosis method for lithium-ion battery packs in electric vehicles," *IEEE Trans. Power Electron.*, vol. 37, no. 7, pp. 8572–8581, Jul. 2022.

[15] X. Hu, K. Zhang, K. Liu, X. Lin, S. Dey, and S. Onori, "Advanced fault diagnosis for lithium-ion battery systems: A review of fault mechanisms, fault features, and diagnosis procedures," *IEEE Ind. Electron. Mag.*, vol. 14, no. 3, pp. 65–91, Sep. 2020, doi: 10.1109/mie.2020.2964814.

[16] F. Yang, W. Li, C. Li, and Q. Miao, "State-of-charge estimation of lithium-ion batteries based on gated recurrent neural network," *Energy*, vol. 175, pp. 66–75, 2019, doi: 10.1016/j.energy.2019.03.059.

[17] Z. Cui, L. Kang, L. Li, L. Wang, and K. Wang, "A hybrid neural network model with improved input for state of charge estimation of lithium-ion battery at low temperatures," *Renewable Energy*, vol. 198, pp. 1328–1340, 2022, doi: 10.1016/j.renene.2022.08.123.

[18] X. Feng et al., "Online state-of-health estimation for li-ion battery using partial charging segment based on support vector machine," *IEEE Trans. Veh. Technol.*, vol. 68, no. 9, pp. 8583–8592, Sep. 2019, doi: 10.1109/tvt.2019.2927120.

[19] O. Ojo, H. Lang, Y. Kim, X. Hu, B. Mu, and X. Lin, "A neural network based method for thermal fault detection in Lithium-Ion batteries," *IEEE Trans. Ind. Electron.*, vol. 68, no. 5, pp. 4068–4078, May 2021, doi: 10.1109/tie.2020.2984980.

[20] H.-J. Lee, K.-T. Kim, J.-H. Park, G. Bere, J. J. Ochoa, and T. Kim, "Convolutional neural network-based false battery data detection and classification for battery energy storage systems," *IEEE Trans. Energy Convers.*, vol. 36, no. 4, pp. 3108–3117, Dec. 2021, doi: 10.1109/tec.2021.3061493.

[21] L. Yao, Z. Fang, Y. Xiao, J. Hou, and Z. Fu, "An intelligent fault diagnosis method for lithium battery systems based on grid search support vector machine," *Energy*, vol. 214, 2021, Art. no. 118866, doi: 10.1016/j.energy.2020.118866.

[22] Z. Sun, P. Liu, and Z. Wang, "Real-time fault diagnosis method of battery system based on shannon entropy," *Energy Procedia*, vol. 105, pp. 2354–2359, 2017, doi: 10.1016/j.egypro.2017.03.676.

[23] Z. Wang, J. Hong, P. Liu, and L. Zhang, "Voltage fault diagnosis and prognosis of battery systems based on entropy and Z -score for electric vehicles," *Appl. Energy*, vol. 196, pp. 289–302, 2017, doi: 10.1016/j.apenergy.2016.12.143.

[24] Z. Deng, X. Hu, P. Li, X. Lin, and X. Bian, "Data-driven battery state of health estimation based on random partial charging data," *IEEE Trans. Power Electron.*, vol. 37, no. 5, pp. 5021–5031, May 2022.

[25] L. Yao, Z. Wang, and J. Ma, "Fault detection of the connection of lithium-ion power batteries based on entropy for electric vehicles," *J. Power Sources*, vol. 293, pp. 548–561, 2015, doi: 10.1016/j.jpowsour.2015.05.090.

[26] P. Wei and H.-X. Li, "Spatiotemporal entropy for abnormality detection and localization of Li-ion battery packs," *IEEE Trans. Ind. Electron.*, vol. 70, no. 12, pp. 12851–12859, Dec. 2023, doi: 10.1109/tie.2023.3234128.

[27] Z. Mao, X. Gu, J. Li, K. Liu, T. Wang, and Y. Shang, "An applicable minor short-circuit fault diagnosis method for automotive lithium-ion batteries based on extremum sample entropy," *IEEE Trans. Power Electron.*, vol. 39, no. 4, pp. 4636–4644, Apr. 2024.

[28] B. Xia, Y. Shang, T. Nguyen, and C. Mi, "A correlation based fault detection method for short circuits in battery packs," *J. Power Sources*, vol. 337, pp. 1–10, 2017, doi: 10.1016/j.jpowsour.2016.11.007.

[29] H. Jin, Z. Gao, Z. Zuo, Z. Zhang, Y. Wang, and A. Zhang, "A combined model-based and data-driven fault diagnosis scheme for lithium-ion batteries," *IEEE Trans. Ind. Electron.*, vol. 71, no. 6, pp. 6274–6284, Jun. 2024.

[30] H. Jin, Z. Zhang, S. X. Ding, Z. Gao, Y. Wang, and Z. Zuo, "Fault diagnosis for parallel lithium-ion battery packs with main current sensor fault and internal resistance fault," *IEEE Trans. Instrum. Meas.*, vol. 73, 2024, Art. no. 3521210.

[31] Y. Kang, B. Duan, Z. Zhou, Y. Shang, and C. Zhang, "A multi-fault diagnostic method based on an interleaved voltage measurement topology for series connected battery packs," *J. Power Sources*, vol. 417, pp. 132–144, 2019, doi: 10.1016/j.jpowsour.2019.01.058.

[32] B. Xia and C. Mi, "A fault-tolerant voltage measurement method for series connected battery packs," *J. Power Sources*, vol. 308, pp. 83–96, 2016, doi: 10.1016/j.jpowsour.2016.01.057.

[33] B. Xia, T. Nguyen, J. Yang, and C. Mi, "The improved interleaved voltage measurement method for series connected battery packs," *J. Power Sources*, vol. 334, pp. 12–22, 2016, doi: 10.1016/j.jpowsour.2016.09.167.

[34] Y. Kang, B. Duan, Z. Zhou, Y. Shang, and C. Zhang, "Online multi-fault detection and diagnosis for battery packs in electric vehicles," *Appl. Energy*, vol. 259, 2020, Art. no. 114170, doi: 10.1016/j.apenergy.2019.114170.

[35] Z. Li, Y. Yang, L. Li, and D. Wang, "A weighted Pearson correlation coefficient based multi-fault comprehensive diagnosis for battery circuits," *J. Energy Storage*, vol. 60, 2023, Art. no. 106584, doi: 10.1016/j.est.2022.106584.

[36] J. Xie, H. Peng, Z. Li, G. Wang, and X. Li, "Data-driven diagnosis of multiple faults in series battery packs based on cross-cell voltage correlation and feature principal components," *IEEE J. Emerg. Sel. Topics Power Electron.*, vol. 11, no. 1, pp. 109–119, Feb. 2023, doi: 10.1109/jestpe.2021.3133879.

[37] G. Wang, G. Zhao, J. Xie, and K. Liu, "Ensemble learning-based correlation coefficient method for robust diagnosis of voltage sensor and short-circuit faults in series battery packs," *IEEE Trans. Power Electron.*, vol. 38, no. 7, pp. 9143–9156, Jul. 2023, doi: 10.1109/tpel.2023.3266945.
[38] S. Zhou, Z. Chen, D. Huang, and T. Lin, "A fault-tolerant SoC estimation method for series–Parallel connected Li-ion battery pack," *IEEE Trans. Power Electron.*, vol. 36, no. 12, pp. 13434–13448, Dec. 2021, doi: 10.1109/tpel.2021.3086555.
[39] S. Zhou, Z. Chen, and T. Lin, "Lithium-ion battery cell open circuit fault diagnostics: Methods, analysis, and comparison," *IEEE Trans. Power Electron.*, vol. 38, no. 2, pp. 2493–2505, Feb. 2023, doi: 10.1109/tpel.2022.3211568.
[40] Y. Shang, G. Lu, Y. Kang, Z. Zhou, B. Duan, and C. Zhang, "A multi-fault diagnosis method based on modified sample Entropy for lithium-ion battery strings," *J. Power Sources*, vol. 446, 2020, Art. no. 227255, doi: 10.1016/j.jpowsour.2019.227275.
[41] T. Lin, Z. Chen, and S. Zhou, "Voltage-correlation based multi-fault diagnosis of lithium-ion battery packs considering inconsistency," *J. Cleaner Prod.*, vol. 336, 2022, Art. no. 130358, doi: 10.1016/j.jclepro.2022.130358.

Tiantian Lin received the Ph.D. degree in naval architecture and ocean engineering from Shanghai Jiao Tong University, Shanghai, China, in 2024.

Her current research interests include fault diagnosis and fault-tolerant state estimate of batteries.

Ziqiang Chen (Senior Member, IEEE) received the Ph.D. degree in mechanical engineering from Xi'an Jiaotong University, Xi'an, China, in 1999.

Since 2007, he has been with Shanghai Jiao Tong University, Shanghai, China, where he is a Professor in the Department of Ocean and Civil Engineering. His current research interests include system identification and state estimation, fault diagnosis, discrete-event systems, automotive and electric vehicle control, battery management systems, composite energy storage system, intelligent industrial detection, robot application, and intelligent manufacturing.

Shiyao Zhou received the Ph.D. degree in naval architecture and ocean engineering from Shanghai Jiao Tong University, Shanghai, China, in 2024.

His current research interests include the areas of the hybrid power system energy management and battery fault-tolerant state estimate.